



**HAL**  
open science

## GPS-derived interseismic coupling on the subduction and seismic hazards in the Atacama region, Chile

Marianne Métois, C Vigny, A Socquet, A Delorme, Sylvain Morvan, I Ortega,  
C.-M Valderas-Bermejo

► **To cite this version:**

Marianne Métois, C Vigny, A Socquet, A Delorme, Sylvain Morvan, et al.. GPS-derived interseismic coupling on the subduction and seismic hazards in the Atacama region, Chile. *Geophysical Journal International*, 2013, 10.1093/gji/ggt418 . hal-01360433

**HAL Id: hal-01360433**

**<https://hal.science/hal-01360433v1>**

Submitted on 5 Sep 2016

**HAL** is a multi-disciplinary open access archive for the deposit and dissemination of scientific research documents, whether they are published or not. The documents may come from teaching and research institutions in France or abroad, or from public or private research centers.

L'archive ouverte pluridisciplinaire **HAL**, est destinée au dépôt et à la diffusion de documents scientifiques de niveau recherche, publiés ou non, émanant des établissements d'enseignement et de recherche français ou étrangers, des laboratoires publics ou privés.

# GPS-derived interseismic coupling on the subduction and seismic hazards in the Atacama region, Chile

M. Métois,<sup>1,2</sup> C. Vigny,<sup>1</sup> A. Socquet,<sup>3</sup> A. Delorme,<sup>2</sup> S. Morvan,<sup>4,\*</sup> I. Ortega<sup>5</sup>  
and C.-M Valderas-Bermejo<sup>5</sup>

<sup>1</sup>Laboratoire de géologie, Ecole Normale Supérieure, 24 rue Lhomond, UMR 8538 du CNRS, F-75005 Paris, France. E-mail: metois@ipgp.fr

<sup>2</sup>Laboratoire de tectonique et mécanique de la lithosphère, Institut de Physique du Globe de Paris, Sorbonne Paris Cité, Univ Paris Diderot, UMR 7154 du CNRS, 1 rue Cuvier, F-75005 Paris, France

<sup>3</sup>ISTerre, UMR 5275 du CNRS, Université Joseph Fourier - Grenoble I, F-38041 Grenoble, France

<sup>4</sup>Laboratoire de Géologie, UMR 8538, École Normale Supérieure, Paris, France

<sup>5</sup>Centro Sismológico Nacional, Universidad de Chile, Santiago, Chile

Accepted 2013 October 8. Received 2013 October 7; in original form 2013 June 13

## SUMMARY

The Atacama region (between 29°S and 25°S) is located in the North-Central area of Chile, a tectonically complex transition area between North and Central Chile. Deformation in Atacama is due mainly to elastic loading on the subduction interface but also to diffuse shortening in the Sierras Pampeanas, Argentina. The seismicity of the subduction is complex in this region: seismic swarms often occur, moderate ( $M_w \sim 6$ ) to large ( $M_w \sim 7$ ) earthquakes occur repeatedly and finally, megathrust earthquakes of magnitudes significantly larger than 8 occur once in a while, the last one being in 1922—almost a century ago. We use new GPS data we collected in the Atacama region between 2008 and 2012 to complete and densify existing data we acquired since 2004 in North-Central Chile. These new data allow to quantify the motion of the Andean sliver and assess the kinematic coupling on the subduction interface at these latitudes. We find that only 7 per cent of the whole convergence motion is taken up by an eastward rotation of the rigid sliver. A large part of the remaining 93 per cent (approximately  $6 \text{ cm yr}^{-1}$ ) gives way to accumulation of elastic deformation in the upper plate, due to locking on the plate interface. This accumulation shows important along-strike and along-dip variations, interpreted in terms of variable coupling which we correlate with seismicity. We identify two areas of low coupling near the ‘La Serena’ (30°S) and ‘Baranquilla’ (27.5°S) bays. Both are correlated with the subduction of singular bathymetric features and seem to stop the propagation of large seismic ruptures. These zones are also seismic swarm prone areas, which seem to occur rather on their edges. These low coupling areas separate two seismic segments where coupling is high: the Atacama segment ( $\sim 100 \text{ km}$  long between 29°S and 28°S) and the Chañaral segment ( $\sim 200 \text{ km}$  long between 27°S and 25°S). Should they rupture alone, these segments are sufficiently coupled and apparently since long enough, to produce  $M_w \sim 8$  events. However, a collective failure of both segments could generate a megathrust earthquake of magnitude close to 8.5, similar to the 1819 and 1922 complex events, which produced important tsunamis. Such giant events may occur in the area once a century.

**Key words:** Satellite geodesy; seismic cycle; Earthquake interaction, forecasting, and prediction; Subduction zone processes; South America.

## 1 INTRODUCTION

The North-Central Chile area (34°–25°S) is a singular portion of the subduction zone between the Nazca and South American plates

\* Now at: EOST, Université de Strasbourg, 5, rue Descartes, F-67084 Strasbourg, France.

( $\sim 68 \text{ mm yr}^{-1}$  Angermann & Klotz 1999; Vigny *et al.* 2009) that remains poorly known, in particular north of 30°S, since few geological and geophysical studies have been conducted there. This zone is a kinematic and tectonic transition between Central Chile where the subduction entirely accommodates the plate convergence (e.g. Métois *et al.* 2012), and North Chile where backarc shortening in the sub-Andean fold-and-thrust belt accommodates about

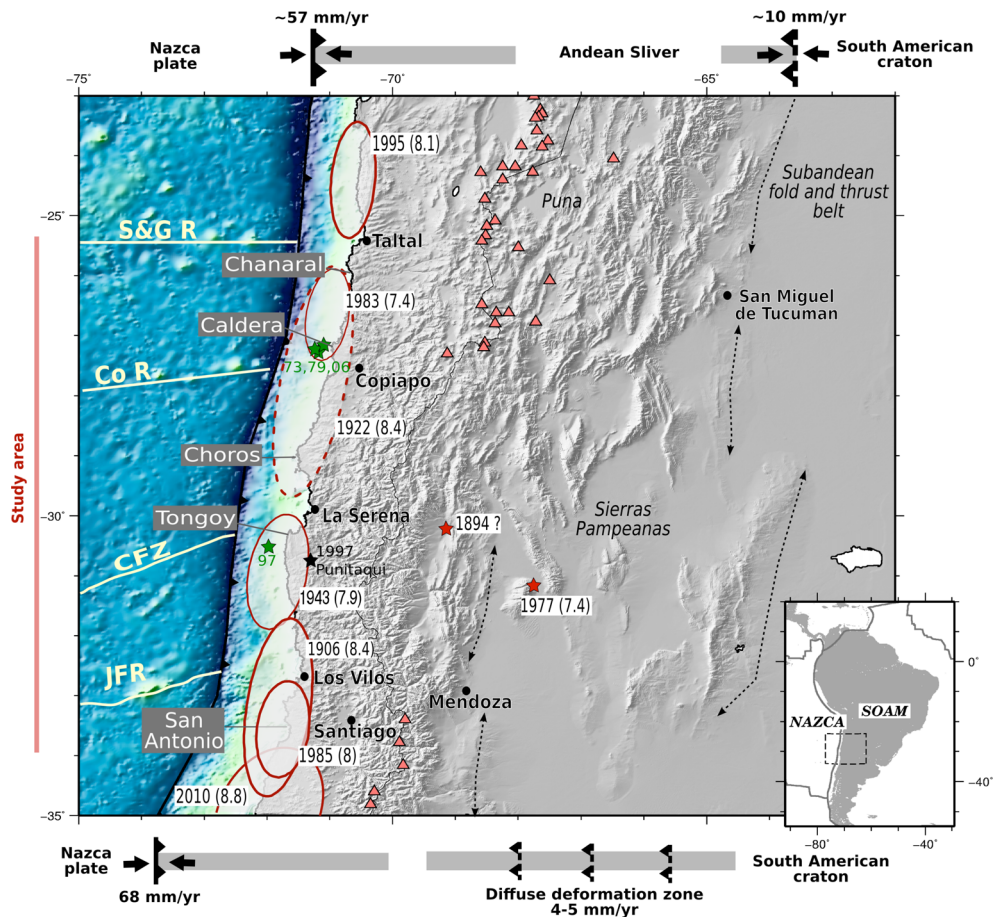


**Figure 1.** Seismotectonic background of the North-Central Chile area and main geological features. Topography and bathymetry are from ETOPO1. The multiple fronts of the Sierras Pampeanas are visible in the shaded DEM and marked with black dashed lines. White lines: contours of bathymetric features of the Nazca subducting plate. S&G R: Salar y Gómez ridge; Co R: Copiapo Ridge; CFZ: Challenger Fracture Zone; JFR: Juan Fernandez Ridge. Red contoured ellipses: maximal rupture zones of the main historical (dashed) and instrumental (solid) megathrust earthquakes since 1800 (Comte & Pardo 1991; Comte *et al.* 2002; Lomnitz 2004). Green stars: hypocentre of the main shock of detected seismic swarms (Holtkamp *et al.* 2011; Ducret *et al.* 2012). Black star: hypocentre of the compressional intraslab 1997 Punitaqui event (Gardi *et al.* 2006; Vigny *et al.* 2009). Red stars: epicentres of the 1894 San Juan and 1977 Caucece earthquakes. Peninsulas and coastal features are named on the grey rectangles. The upper and bottom diagrams represent the three-plate model configuration at the Northern and Southern edges of the study area, respectively. Grey areas mark the supposed extent of elastic deformation above the subduction megathrust and in the Sierras Pampeanas.

15 per cent of the plate convergence (e.g. Brooks *et al.* 2011; Métois *et al.* 2013). In North-Central Chile, the continuous and well-marked sub-Andean front vanishes and a series of thrusts develop to form the Sierras Pampeanas, that narrow south of 34°S (Fig. 1 and Jordan & Allmendinger 1986). Even if some of these thrusts are active structures with a moderate level of past and present shallow seismicity (Figs 1 and 2 and Kadinsky-Cade *et al.* 1985), it is not clear whether this large zone of diffuse deformation accommodates a significant part of the plate convergence motion, generating an Andean sliver with a distinct motion from the South American craton (Brooks *et al.* 2003; Vigny *et al.* 2009; Métois *et al.* 2012). Should this sliver exist, its motion would be difficult to be defined within the interseismic period since this signal of only several millimetres per year could be hidden, or at least altered, by coupling variations on the subduction interface. North-Central Chile is also characterized by an unusual behaviour of the subduction zone itself since the slab flattens at  $\sim 100$  km depth from 32°S to 26°S (Tassara *et al.* 2006; Pardo *et al.* 2012) and that no volcanic activity is observed in this so-called ‘flat slab’ area (Fig. 1). Four bathymetric features (ridges or fracture zones) that are subducting within the area could also play a role in the subduction process, from south to north: the

Juan-Fernandez ridge, the Challenger fracture zone, the Copiapó ridge and the Salar y Gómez ridge (Fig. 1).

In North-Central Chile, only two megathrust earthquakes occurred during the previous century: the Valparaíso earthquake of 1906,  $M_w$  8.4 (32°–34.5°S; Beck *et al.* 1998) and the Copiapó earthquake of 1922,  $M_w$  8.4 (26°–30°S; Lomnitz 2004). Since then, several other important earthquakes have occurred, but of lesser magnitude: the  $M_w$  7.9 event ruptured south of La Serena in 1943, the  $M_w$  8.0 1985 earthquake ruptured again in front of Valparaíso and two earthquakes of  $M_w \sim 7.8$  ruptured the subduction interface from 26°S to 27.5°S in 1946 and 1983. Finally, several seismic swarms occurred in the region: near Caldera (27°S) in 1973, 1979 and 2006; near Tongoy (31°S) in 1997 (Holtkamp *et al.* 2011) and possibly near La Serena (29°S) presently. At the southern edge of our study area, the seismicity in front of Valparaíso is complex and in particular the relations between the events of 1906, 1985 and the 2010 Maule earthquake are not clear. If 1906 and 2010 are doubtlessly megathrust earthquakes whose ruptures seem to connect well with no or limited overlap, the 1985 smaller Valparaíso earthquake is not easy to place in the sequence. At the northern end of our study area, the rupture zone of the 1922 earthquake seems

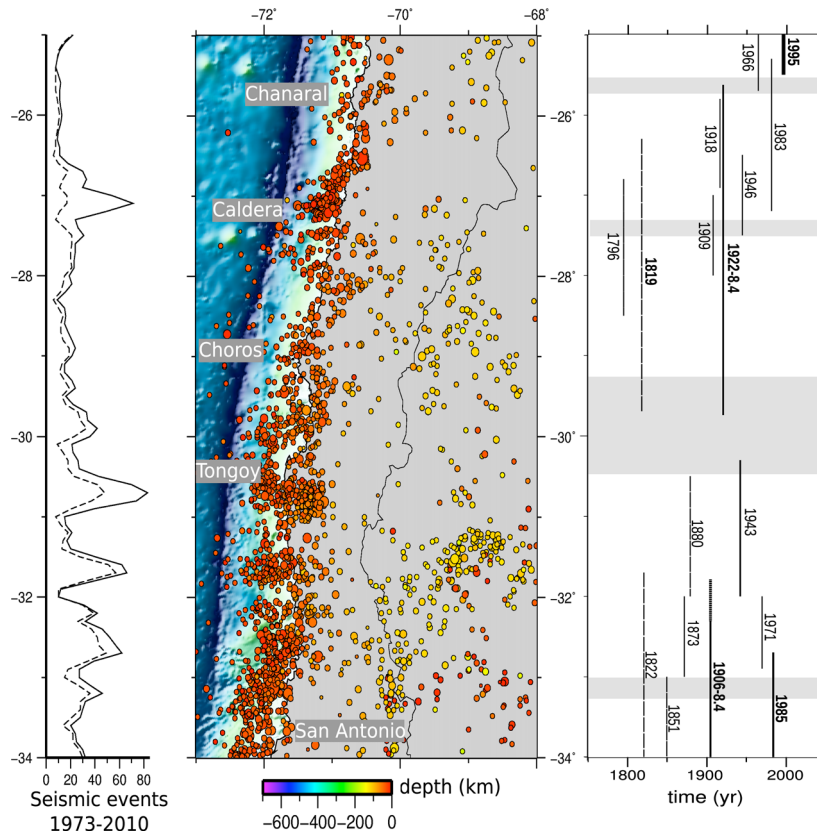


**Figure 2.** Left panel: plain line depicts the number of  $4.5 < M_w < 7$  shallow earthquakes ( $z < 60$  km, upper-plate crustal earthquakes being excluded) recorded by the USGS catalogue from 1973 to 2010 in North-Central Chile, and calculated on  $0.2^\circ$  of latitude sliding windows. Dashed line: same but excluding swarms-related events and aftershocks of the 1985 earthquake. Centre panel: map of  $4.5 < M_w < 7$  earthquakes registered by USGS for the same period of time. Right panel: estimated rupture zones of major subduction earthquakes since 1800. Grey areas mark potential barriers to seismic propagation.

to correspond well to the highly coupled Atacama segment defined by Métois *et al.* (2012). This region has not ruptured since then and shows little background seismicity since 1973 (Fig. 2), that is very similar to what was observed in the Maule area, before 2010. Therefore, we consider that this area could be a mature seismic gap where the deformation accumulated at a steady state of  $\sim 7$  cm  $\text{yr}^{-1}$  over 90 yr could potentially already reach the equivalent of 6 m of slip-deficit assuming full coupling on the entire surface of the segment. If released at once over an  $\sim 300$ -km-long segment, such amount of slip would correspond to an earthquake of magnitude larger than 8. To assess the seismic hazard of this area, a precise determination of the segment boundaries and of the amount and distribution of coupling is necessary. Previous studies already identified strong coupling variations along the Chilean subduction zone (e.g. Métois *et al.* 2012, 2013). In particular, a large zone of weak coupling had been identified near  $30^\circ\text{S}$  (La Serena), which separates two highly coupled segments: the Metropolitan region to the south, and the Atacama region to the north. However, sparse data north of  $30^\circ\text{S}$  impeded a good resolution of the coupling distribution north of La Serena.

In this study, we use new campaign GPS data acquired between 2008 and 2012 between  $30^\circ\text{S}$  and  $24^\circ\text{S}$  (Fig. 3) to (i) test the hypothesis of an Andean microplate (or sliver) motion at these latitudes, and (ii) quantify accurately the coupling distribution on the subduction interface. For this purpose, we invert this new velocity field simultaneously for the motion of the Andean sliver (the position and rate of its Euler pole) and the coupling distribution on the subduction interface using an elastic backslip code.

## 2 GPS MEASUREMENTS

For this work, we collected additional data (four campaigns in 2008, 2009, 2010 and 2011) on the network used by Vigny *et al.* (2009) and Métois *et al.* (2012) between  $33^\circ\text{S}$  and  $30^\circ\text{S}$ . In addition, we installed 32 new benchmarks between  $30^\circ\text{S}$  and  $24^\circ\text{S}$  and surveyed this network in 2010, 2011 and 2012. We include in this new network 2 SAGA (South America Geodynamic Activities, see Khazaradze & Klotz 2003) and 3 CAP markers (Central Andes GPS Project, see Brooks *et al.* 2003), and data from 19 regional continuous stations of the French-Chilean network (see Supporting Information).

We reduce these data in 24-hr sessions to daily estimates of station positions using the GAMIT software (release 10.4, King & Bock 2002), choosing the ionosphere-free combination, and fixing the ambiguities to integer values. We use precise orbits from the International GNSS Service for Geodynamics (IGS, Beutler *et al.* 1999) and IGS tables to describe the phase centres of the antennae. We estimate one tropospheric vertical delay parameter per station every 3 hr and used the standard Niell (1996)'s mapping functions. The horizontal components of the calculated relative position vectors are precise to within a few millimetres for all pairs of stations, as measured by the rms scatter about the mean (so-called baseline repeatability, see Table S5).

We combine daily solutions using the GLOBK software Herring (2002) in a 'regional stabilization' approach. To define a consistent reference frame for all epochs, we include tracking data from a selection of 35 permanent stations in South America, 10 of them belonging to the IGS (Beutler *et al.* 1999). 31 stations span the



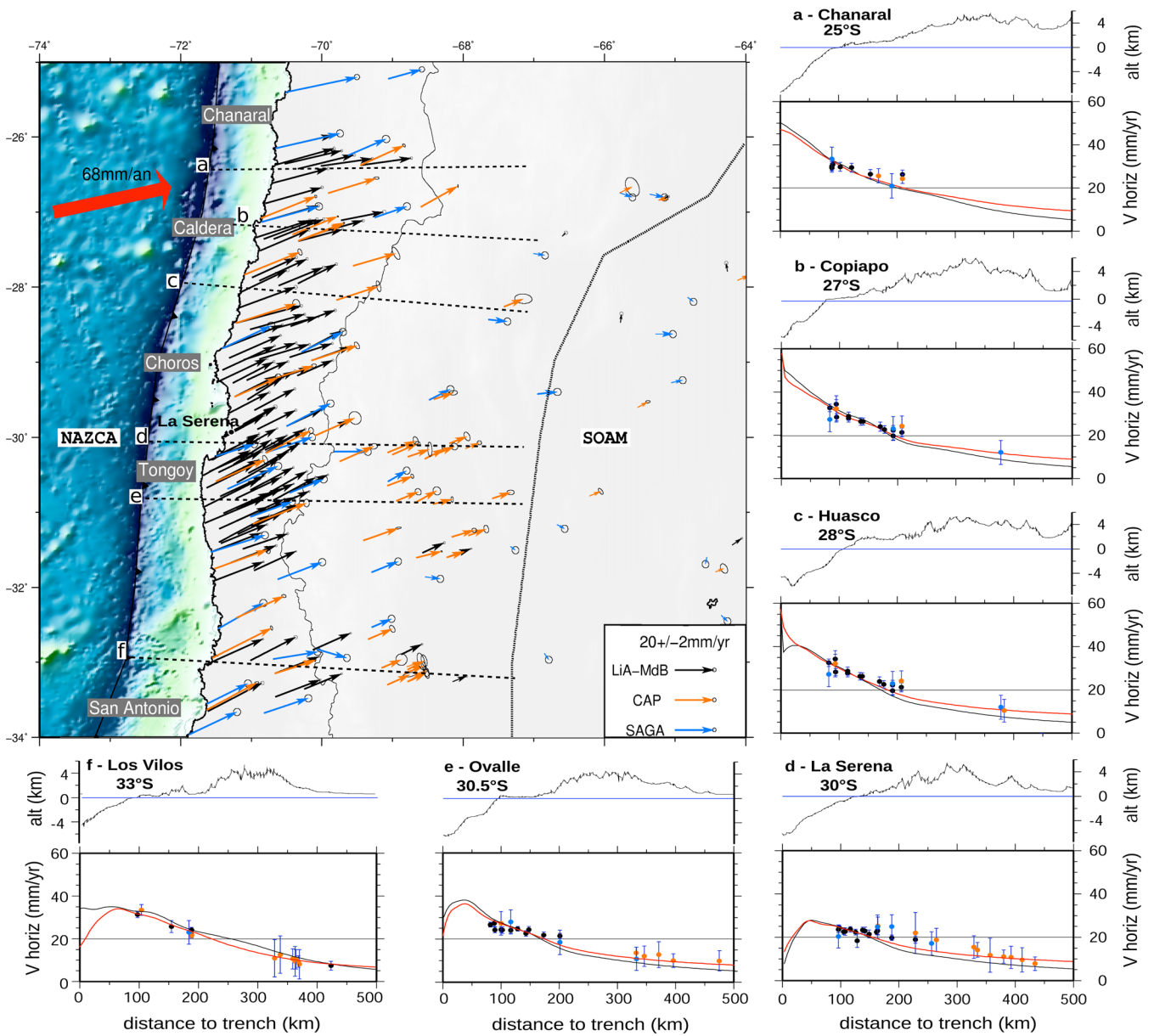


**Figure 3.** New interseismic data set acquired between 2004 and 2012 on campaign benchmarks and permanent stations (black arrows), together with previously published data sets (orange: CAP; blue: SAGA). Velocities are plotted in the NNR-Nuvel1A fixed South America reference frame (Table S1). Dotted grey line: eastern limit of the inferred Andean sliver block. Around the map, boxes with topography (in km) and horizontal velocities (in  $\text{mm yr}^{-1}$ ) plotted against the distance to the trench (in km) along six 30-km-width trench-normal profile lines (dashed lines on the map). Black curve: deformation predicted by the two-plate model; red curve: deformation predicted by our preferred three-plate model presented in Fig. 5.

South American craton in Brazil (RBMC network), Guyana and Argentina (RAMSAC network), and two stations sample the Nazca plate (see Table S2). This combination step is more complex than usual because the 2010  $M_w$  8.8 Maule earthquake affected part of the North-Central Chile area. Coseismic jumps of several millimetres were detected at all sites, and post-seismic rebound is negligible only north of 30°S (Fig. S1 and Vigny *et al.* 2011). Therefore, we decided not to include the post-Maule measurements in our velocity combination for benchmarks located south of 30°S. Furthermore, they were often measured before the earthquake (around 10 times before 2010) and their interseismic velocity was already determined with sufficient accuracy. North of 30°S, we apply the coseismic jumps estimated by Vigny *et al.* (2011) on the permanent stations of our network, and compute the theoretical deformation produced on

each benchmark using triangulation interpolation (see Supporting Information). Thus, we corrected the time-series of the affected sites and combine all surveys between 2004 and 2012 to constrain an interseismic velocity at all points. Finally, we had to reject the majority of post-2010 data at southern Argentine permanent stations since they are experiencing large post-seismic trenchward motion.

We combine daily solutions using Helmert transformations to estimate translation, rotation, scale and Earth orientation parameters (polar motion and UT1 rotation). This ‘stabilization’ procedure defines a reference frame by minimizing, in the least-square sense, the departure from the *a priori* values determined in the International Terrestrial Reference Frame 2008 (ITRF, Altamimi *et al.* 2011). In this procedure, height and height rates weight is 10 times lower than for horizontal component of position and

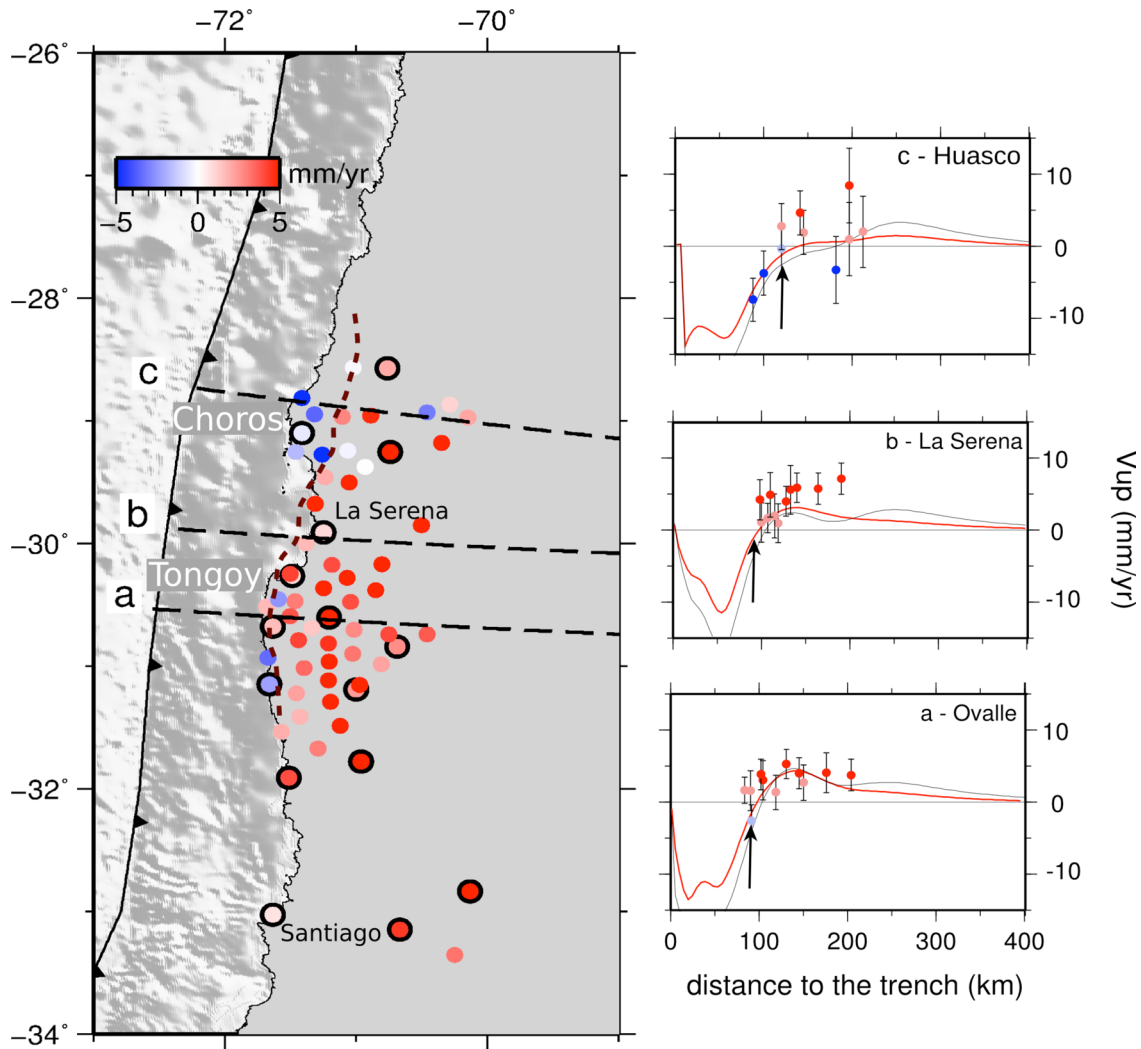


**Figure 4.** Left-hand side: vertical data set used in this study. Uplift (red) and subsidence (blue) amplitudes are colour coded ( $\text{mm yr}^{-1}$ ). Bold contoured dots are continuous cGPS stations. Brown dashed curve: potential location of the hinge line. Right-hand side: vertical deformation in  $\text{mm yr}^{-1}$  along three profile lines plotted on the map (dashed lines). Tick marks: scaled uncertainties. Predicted vertical deformation is plotted for our preferred three-plate (red bold curve) model and two-plate (thin black curve) models. Black arrow: location of the hinge line.

velocity. This procedure estimates the positions and velocities for a set of nine well-determined stations unaffected by the Maule earthquake in the stable part of the South American Continent (KOUR, POVE, CUIB, CHPI, RIO2, BRAZ, BRFT and ISPA). The misfit to these ‘stabilization’ stations is  $0.3 \text{ mm}$  in position and  $2.1 \text{ mm yr}^{-1}$  in velocity (see Fig. 2). Thus, we obtain an horizontal velocity field in the ITRF 2008 that we plot relative to the South American Plate defined by the NNR-Nuvel-1A model (DeMets 1994;  $25.4^\circ \text{S}$ ,  $124.6^\circ \text{S}$ ,  $0.11^\circ \text{ Myr}^{-1}$ , see Fig. 3). In addition, and because we have long time-series constrained by numerous measurements, we selected 72 reliable vertical velocities based on the following quality criteria: We rejected the velocities based on less than 2-yr time span measurements or less than three measurements, the velocities with uncertainties larger than  $4.5 \text{ mm yr}^{-1}$  or with normalized rms greater than 2, unrealistic high velocities (uplift larger than  $10 \text{ mm yr}^{-1}$  for Andean sites), and velocities from survey sites that differ significantly from those of nearby cGPS stations (Fig. 4 and the Supporting Information).

We combine this new GPS data set with previously published SAGA and CAP GPS horizontal velocities in the area (Brooks *et al.* 2003; Khazaradze & Klotz 2003), that we rotate in our reference

frame following Métois *et al.* (2012). On the several common markers shared with CAP and SAGA data sets, the interseismic velocities have in general the same orientation but oldest data sets exceed our velocities by as much as  $5 \text{ mm yr}^{-1}$  in some places and by  $3 \text{ mm yr}^{-1}$  on average. This discrepancy is observed mainly for the most inland points of our network, while velocities are very similar at the coast. Furthermore, north of our network, the CAP and SAGA velocities exhibit a more northward pattern for the inland points than ours. This may be due to the fact that these data were acquired during the 1993–2001 and 1994–1997 time spans, respectively, implying that the northernmost points could have been affected by the coseismic motion of the 1995 Antofagasta earthquake (Fig. 1). Therefore, we decided to include these old measurements in our inversion since they measure the far-field deformation, but we decrease their weight relative to our recent and more reliable interseismic data.

### 3 DATA ANALYSIS

The general pattern of the horizontal surface deformation near the trench is typical of interseismic loading on the subduction interface:

horizontal velocities decrease rapidly in the first 200 km from the trench, and slowly decrease going inland with a clockwise rotation towards a trench-normal direction (Fig. 3). However, the far-field horizontal velocities are higher than  $5 \text{ mm yr}^{-1}$  until a distance of 500 km from the trench and fall to zero only on the South American craton. This could be representative of a small motion of the Andean sliver or to internal deformation within the Andes. Still, this far-field pattern is much less clear than what is observed in central Andes (i.e. North Chile and Bolivia) where a block motion of  $\sim 10\text{--}13 \text{ mm yr}^{-1}$  is necessary to fit the horizontal data (e.g. Brooks *et al.* 2011; Chlieh *et al.* 2011; Métois *et al.* 2013). The main variation to the typical interseismic loading pattern is observed in the La Serena bay ( $30^\circ\text{S}$ ) where the horizontal coastal velocities are lower than everywhere else by almost  $10 \text{ mm yr}^{-1}$  and almost no shortening is observed in the near field (from 100 to 200 km from the trench). This pattern already indicates that coupling is very weak in the La Serena area, and is higher everywhere else.

The vertical surface displacements (Fig. 4) indicate that the hinge line (i.e. the line that marks the change from subsidence to uplift at surface) is beneath the coast south of  $30^\circ\text{S}$ , and comes inland north of  $29^\circ\text{S}$ . Before the 2010  $M_w$  8.8 megathrust earthquake, the hinge line was also observed inland along the Maule segment and was considered as a proxy for the downdip extent of the significantly (more than  $\sim 50$  per cent) coupled portion of the interface (Ruegg *et al.* 2009). We therefore interpret the coastal subsidence north of Choros ( $29.2^\circ\text{S}$ ) as the sign of a large and deep highly coupled zone. In any case, the northern limit of the La Serena low-coupling intersegment correlates with the end of the bay, near Choros.

#### 4 MODELLING STRATEGY

We quantify the kinematic coupling coefficient  $\Phi$  following the method described in Métois *et al.* (2012), based on the elastic back-slip DEFNODE code developed by McCaffrey (2002). Doing so, we consider that the deformation is purely elastic and we neglect the viscous effects that may occur during the interseismic loading phase. This assumption is reasonable since most of our data are located in the near-field relative to the trench where elastic deformation dominates. In all models, the total convergence between the Nazca and South American plates is fixed and corresponds to the relative pole ( $55.9^\circ\text{N}$ ,  $95.2^\circ\text{W}$ ,  $0.610^\circ \text{ M yr}^{-1}$ ) published by Vigny *et al.* (2009), which yields  $68 \text{ mm yr}^{-1}$  at  $30^\circ\text{S}$ , still slower than the recently published MORVEL estimate (DeMets *et al.* 2010, and Supporting Information). We use the simple planar geometry from Métois *et al.* (2012) with a  $20^\circ$  dipping slab down to 100 km depth for the flat-slab area (from  $32^\circ\text{S}$  to  $26^\circ\text{S}$ ), and a smooth transition towards a  $15^\circ$  dipping slab in the southernmost part of the region ( $34^\circ\text{S}$ ). The interface is meshed with a grid of nodes with a  $0.25^\circ$  latitudinal and 22 km along-dip grid-steps (544 nodes, 353 being associated to variable values of kinematic coupling). We impose an along-strike smoothing coefficient linearly increasing with depth in our inversions to avoid numerical instabilities. We also choose to taper the coupling coefficient to zero for the nodes deeper than 80 km depth in all models, while no tapering is applied in the updip direction. Both our two-plate (without sliver) and three-plate (with sliver) preferred models (Fig. 5) are obtained using a smoothing coefficient of 0.7 per latitude degree linearly increasing with depth as it yields the best compromise between smoothing and normalized rms (see the Supporting Information). In order to avoid edges effects, we impose similar coupling on the last two columns of nodes on the grid tips as suggested by McCaffrey (2002).

We estimate the sensitivity of our network by calculating the sum of the displacements at GPS stations due to unit strike and dip-slip on each node (see the Supporting Information and Loveless & Meade 2011). This shows that new interseismic velocities in the northern part of our network improve the sensitivity to coupling between 10 and 60 km depth. Additional measurements are still needed north of Huasco ( $28.5^\circ\text{S}$ ) to precise the vertical velocities there and confirm the along-strike extension of the highly coupled zone detected by the horizontal velocities. The resolution decreases beneath the main Cordillera where little GPS data are available. Overall, in North-Central Chile, the coast is relatively close to the trench compared to other subduction zones (70 km in the Tongoy and Choros peninsulas), and therefore the sensitivity of our network is good up to  $\sim 10$  km depth. Unresolved regions of the interface, such as edges of the grid and shallowest interface, are masked in Fig. 5.

#### 4.1 Two- and three-plate models

We first invert for the coupling coefficient on the subduction interface in the framework of a simple two-plate model where 100 per cent of the convergence is localized on the subduction zone. This model fails in retrieving simultaneously the horizontal deformation in the far field (normalized rms for horizontal data is 2.08) and the vertical velocities (normalized rms for vertical data is 2.91, see Figs 5a and b). It produces resolvable (more than  $5 \text{ mm yr}^{-1}$ ) and systematic northeastward residuals starting 200 km away from the trench and extending to the Sierras Pampeanas easternmost front ( $\sim 66^\circ\text{W}$ ).

Then an Andean sliver is introduced in order to absorb a small part of the convergence. It is bounded by the subduction trench to the west and by the most eastward thrust front of the Sierras Pampeanas ( $\sim 66^\circ\text{W}$ ) that connects with the sub-Andean fold-and-thrust belt at  $25.6^\circ\text{S}$  to the east (Fig. 1). Our purpose here is not to identify the boundaries of this block and to determine the distribution of the convergence on the numerous fold and thrusts in Argentina where we have few data. We rather aim at removing the contribution of this sliver motion to the net budget of the velocity field in the region affected by elastic loading on the subduction interface. We invert simultaneously for the coupling distribution on the subduction interface and for the rotation motion of such a sliver (Figs 5c and d). Our preferred three-plate model yields a much better fit to both vertical and horizontal data sets (hrms is 1.68 and vrms is 2.11), even if some northeastward residuals are still observed inland north of  $32^\circ\text{S}$  (in particular in the SAGA and CAP data sets). These residuals may be associated to elastic loading on local thrusts accommodating the diffuse deformation (parameters that are not included in our model). The sliver motion is best described by the Eulerian pole ( $39.2^\circ\text{S} \pm 2$ ,  $61.5^\circ\text{W} \pm 2$ ,  $-0.25^\circ \text{ M yr}^{-1} \pm 0.1$ ) located in the South Atlantic ocean, that is very close to the one inverted for the Andean sliver in North Chile by Métois *et al.* (2013;  $48.6^\circ\text{S}$ ,  $47.8^\circ\text{W}$ ,  $-0.19^\circ \text{ M yr}^{-1}$ ). This motion almost corresponds to a northeastward translation that produces  $\sim 5 \text{ mm yr}^{-1}$  of shortening on average, with a slight decrease of  $2 \text{ mm yr}^{-1}$  from north to south that yields almost no shortening in the Metropolitan area ( $34^\circ\text{S}$ ). These findings are consistent with geodetic studies in the Sierras Pampeanas that estimate a shortening rate of  $4\text{--}10 \text{ mm yr}^{-1}$  at  $31^\circ\text{S}$  (Kadinsky-Cade *et al.* 1985; Brooks *et al.* 2003), and with geological long-term reconstructions that predict an important decrease in the shortening amount from north to south (McQuarrie 2002; Arriagada *et al.* 2008).

Our best three-plate model differs from the coupling distribution previously published by Métois *et al.* (2012) by the fact that we

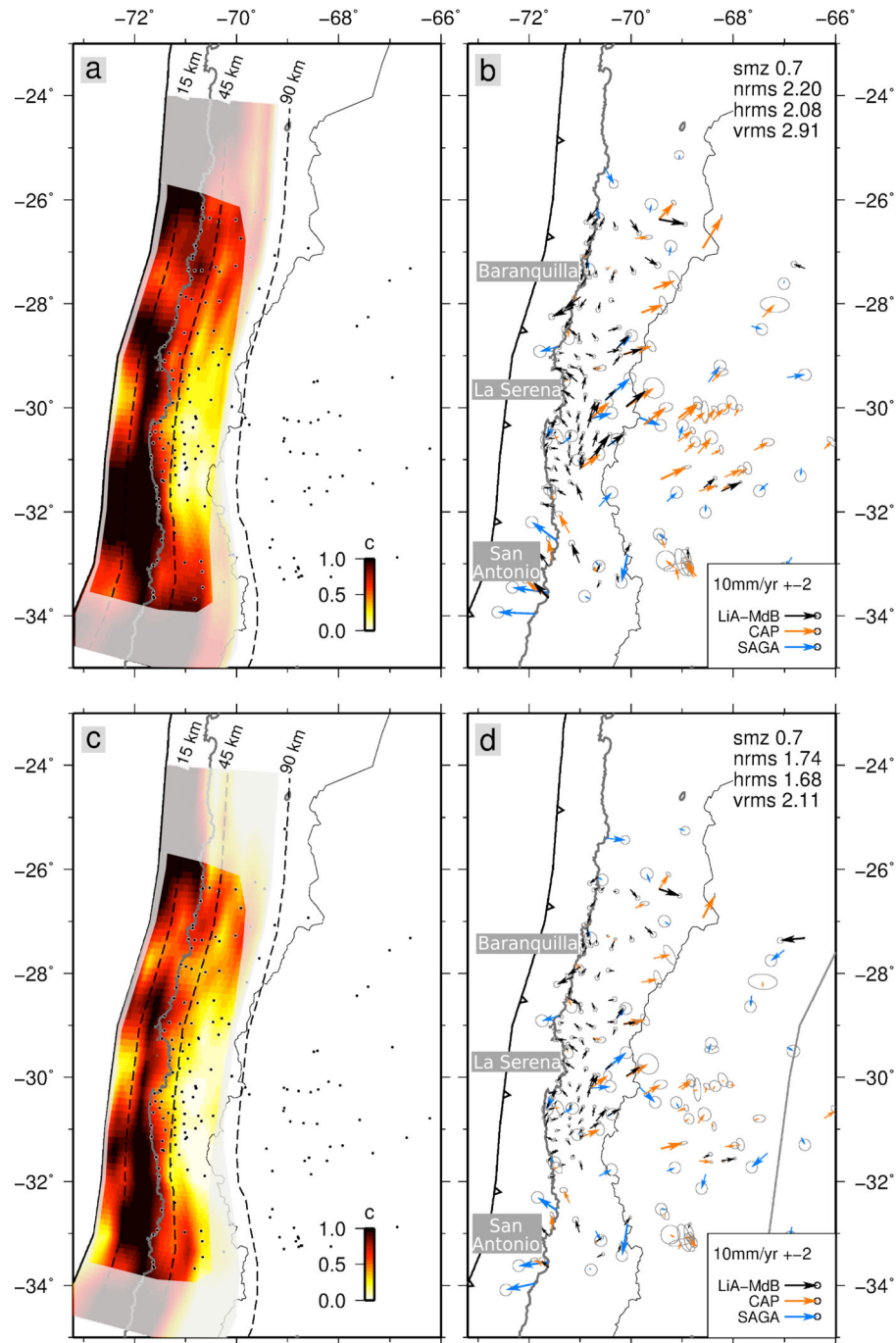


**Figure 5.** Coupling distributions (left-hand side) and associated residuals (right-hand side) of the two-plate (a and b) and three-plate preferred models (c and d). The smoothing coefficient and normalized rms (relative to horizontal hrms or vertical vrms data) are indicated in the right corner box. Left-hand side: the coupling coefficient value (from 0 per cent to 100 per cent) is colour coded from white to black through yellow and red. Greyish areas are zones where we lack resolution (i.e. areas where the discrepancy between the initial checkerboard coupling distribution and the inverted one is greater than 30 per cent). Dashed curves are slab isodepths whose values are indicated at the northern end of the slab (km). Black dots show the locations of GPS sites. Right-hand side: residuals are colour coded relative to their data set. Black line in (d): eastern limit of the Andean sliver block.

include new data, we allow for a sliver motion and we impeded coupling below 80 km. Sliver motion and very deep coupling can both generate the far-field eastward motion observed in the data. However, since deep coupling is physically unlikely, we conclude that the deepest highly coupled patches of the model published by Métois *et al.* (2012) are model artefacts, which are eliminated by taking into account the sliver motion. It is to note that in our modelling, we do not take into account viscous deformation that

could be occurring in the middle to far field from the trench, and notably in the diffuse deformation area of the Sierras Pampeanas.

#### 4.2 Pattern of interseismic coupling

Since 7 per cent of the whole convergence motion ( $68 \text{ mm yr}^{-1}$  at this latitude) is accommodated elsewhere than on the subduction, the average coupling coefficient over the entire region is lower for



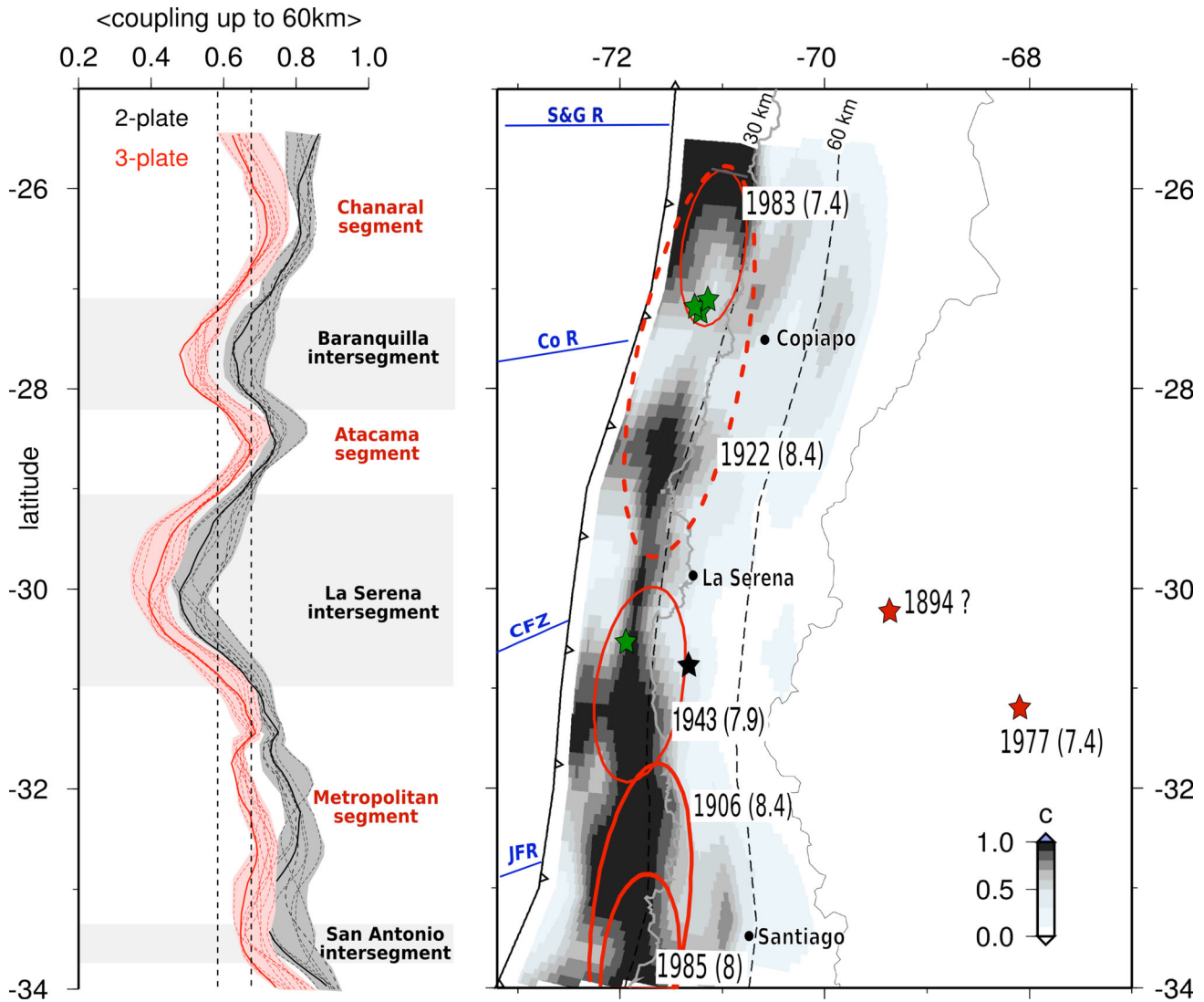


**Figure 6.** Left-hand side: average coupling coefficient versus latitude.  $\langle\Phi\rangle$  is the integration from 0 to 60 km depth of the coupling distribution on the interface, using a  $0.5^\circ$  sliding window in latitude. Greyish curves are for the two-plate model, reddish curves are for the three-plate model. Solid curves depict the preferred (best-fit) model, and dashed curves depict a subset of alternative models with reasonably good nrms ( $<2.8$  for two-plate models, and  $<2$  for three-plate models). Grey and pink shaded areas depict the envelope of these alternative models and represent the uncertainty of our preferred coupling distributions. Black dotted lines mark the mean value of coupling for each case. Segments (i.e. where  $\langle\Phi\rangle$  is larger than the mean value) and intersegment zones ( $\langle\Phi\rangle$  lower than the mean value) are named on the right-hand side of the graph. Right-hand side: coupling distribution is colour coded and superimposed with estimates of the rupture zones of major instrumental or historical earthquakes (solid or dotted red ellipses, respectively). Green stars: swarm events registered since 1970; red stars: major shallow thrust earthquakes in the Sierras Pampeanas; black star: 1997 Punitaqui compressionnal intraslab earthquake. Dark blue solid line: rough contours for the Salar y Gómez Ridge (S&G R), Copiapó Ridge (Co R), Challenger Fracture Zone (CFZ) and Juan Fernandez Ridge (JFR).

the three-plate model (61 per cent) than for the two-plate model (72 per cent). However, beside this discrepancy, both models share similar lateral variations of the average coupling  $\langle\Phi\rangle$  integrated from surface to 60 km depth (Fig. 6). Overall, from  $34^\circ\text{S}$  to  $31^\circ\text{S}$ , coupling is high down to 40 km depth (more than the average value) and its average value gradually decreases going north. Then, at  $31^\circ\text{S}$ , beneath the Tongoy Peninsula,  $\langle\Phi\rangle$  becomes lower than average and decreases sharply to as low as 40 per cent in the centre of the La Serena Bay ( $30^\circ\text{S}$ ). Passed the bay, coupling increases again going north, up to the average value beneath Choros ( $29^\circ\text{S}$ ) where a narrow highly coupled zone develops down to 35–40 km depth and a 5- to 10-km-wide intermediate coupling zone develops underneath. This high coupling patch ends at  $28.2^\circ\text{S}$  where coupling decreases again and reaches a local minimum of 50 per cent in front of Copiapó

and the Baranquilla bay ( $27.5^\circ\text{S}$ ). Going north, a highly coupled zone develops again north of the Caldera Peninsula, from surface to 30 km depth, and extends at least up to  $25^\circ\text{S}$ . Its northern limit is still out of the resolved portion of our model.

## 5 DISCUSSION

Based on the along-strike variations of the average interseismic coupling  $\langle\Phi\rangle$ , we define a segmentation of the megathrust that completes the one published by Métois *et al.* (2012; Fig. 6). We confirm the existence and limits of the Metropolitan segment and find two new segments (where  $\langle\Phi\rangle$  is high), the Atacama ( $29^\circ\text{S}$ – $28.2^\circ\text{S}$ ) and Chañaral ( $27.2^\circ\text{S}$ – $25.5^\circ\text{S}$ ) segments. The three associated

intersegments (where  $\Phi$  is low) are the San Antonio (33.6°S–33.3°S), La Serena (30.8°S–29°S) and Baranquilla (28.2°S–27.2°S) intersegments. In the following, we discuss their mechanical behaviour based on the correlation between historical ruptures and recent interseismic coupling. The Metropolitan segment and the San Antonio intersegment are unchanged with respect to Métois *et al.* (2012). Therefore, we focus here on the northernmost segments (Atacama, Chañaral) where new and denser data provide an extended coupling distribution and better resolution.

### 5.1 Seismic cycle on the coupling segments

Our new data confirm that the ‘Atacama segment’ is a narrow highly coupled zone of approximately 100 km long, between 29°S and 28.2°S, where present-day seismicity is low (Fig. 2). This segment did not rupture since the 1922  $M_w$  8.4 earthquake that produced an important tsunami Lomnitz (2004). Therefore, assuming it has been fully coupled from surface to 40–45 km depth since 1922, the rupture of the Atacama segment alone could produce an  $M_w$  8.0–8.1 subduction earthquake (almost 5.5 m released on a  $100 \times 130$  km<sup>2</sup> fault plane).

The lateral extent of the Chañaral segment remains poorly resolved, since very few interseismic velocities are available in its northern termination (25.5°S). New measurements are needed there to assess whether this segment ends in the Taltal Bay where deep moderate-size earthquakes occurred (e.g. 1966  $M_w$  7.5, Deschamps *et al.* 1980) and where the 1995 Antofagasta earthquake stopped, or if it is continuous with the Paranal segment defined by Métois *et al.* (2013) to the north. Nevertheless, a high coupling zone develops starting from 27.2°S, and extends down to 30 km depth on the subduction interface. Part of the Chañaral segment was ruptured during the 1918, 1946 and 1983 moderate-size events ( $M_w < 7.5$ , Beck *et al.* 1998). However, these moderate events did not produce any tsunami, indicating they probably ruptured only the deepest part of the highly coupled zone (similarly to the 2007  $M_w$  7.7 Tocopilla earthquake, Béjar-Pizarro *et al.* 2010), while large events similar to the 1922 earthquake can rupture the whole interface including its shallower part. Rather than contributing to stress release, the three moderate earthquakes that occurred in the segment during the 20th century brought the overall segment closer to failure by adding to the stress of the shallower part of the interface.

According to historical seismicity, each segment is capable of producing an  $M_w$  close to 8 subduction earthquake, the rupture of which is stopped by the neighbouring intersegments. Such events seem to occur every 30–40 yr in the Chañaral segment, while few earthquakes are reported in the Atacama segment (Fig. 2). The 1819 and 1922 ( $M_w \sim 8.4$ ) megathrust earthquakes that produced devastating tsunamis must have ruptured more than a single segment, if we suppose that the present-day segmentation was already in place. Therefore, they probably correspond to a collective failure of both segments where either the rupture of the first one triggered the rupture of the second one, statically or dynamically, or the rupture initiated in one segment passed across or around the Baranquilla intersegment. In the literature, both events were described as complex ruptures: three different shocks were felt by the population for each of them (Willis & Macelwane 1929; Lomnitz 2004). This is consistent with a successive rupture of Atacama and Chañaral segments. The fact that tsunamis were triggered is also consistent with the resolved coupling observed in the shallow interface (up to 10 km depth) in both segments, which gives way to shallow seismic rupture.

### 5.2 Mechanical behaviour of intersegments

The large intersegment zone located beneath the bay of La Serena correlates with the termination of several major earthquakes (the 1922, 1943, 1880 and possibly 1819 and 1796 events, Beck *et al.* 1998; Comte *et al.* 2002; Lomnitz 2004). It is also the place where the Challenger Fracture Zone enters into subduction. This very low-coupled zone is bounded by a singular coastal feature to the south, the Tongoy Peninsula, and to the north by the Choros area. The Tongoy Peninsula experienced a large seismic swarm in 1997 (Fig. 1) that preceded an unusual intraslab earthquake in Punitaqui (Gardi *et al.* 2006). This may indicate that this area of low apparent coupling is due to interfingering of velocity-strengthening and velocity-weakening patches on the interface, as it has been suggested under the Pisco Peninsula (Perfettini *et al.* 2010). The fact that this area behaves as a barrier to seismic ruptures could be explained if the velocity-strengthening patches, able to slow down the rupture propagation, are dominant. At the same time, the smaller velocity-weakening patches could be responsible for the swarms of small seismic events, and may rather be located on the edges of the intersegment where we observe an abrupt transition between high and very low coupling. Finally, an area where velocity-strengthening behaviour prevails (i.e. where apparent coupling is low) could be prone to episodic transient slow slip. However, none has been captured here since 2004 when the first permanent GPS stations were installed in the La Serena Bay.

The Baranquilla intersegment that forms the boundary between the Atacama and Chañaral segments, is two times narrower than the La Serena intersegment but is also located under a large bay. It correlates with the southern limit of the 1983, 1946 and 1918 moderate earthquakes, and is also where the Copiapó ridge subducts (Comte *et al.* 2002). In the bay, the seismicity relocated by Comte *et al.* (2002) suggests that a conical seamount subducts beneath the bay of Baranquilla and could explain the morphology of the coastline. Therefore, following others (e.g. Scholz & Small 1997; Wang & Bilek 2011), we could explain this low in coupling coefficient by changes in the frictional properties of the interface due to seamount subduction (e.g. fluid pressure, decrease of normal stress). Furthermore, three seismic swarms occurred at the northern edge of the intersegment, in front of the Caldera Peninsula, in 1973, 1979 and 2006 (Fig. 1 and Comte *et al.* 2002; Holtkamp *et al.* 2011). The most recent swarm episode has potentially induced important post-seismic slip on the interface (Ducret *et al.* 2012). Therefore, in the Baranquilla intersegment, like in La Serena, the low apparent coupling value may be due to dominant velocity-strengthening patches on the interface that may act as a barrier for seismic rupture propagation and could creep during inter- and post-seismic phases of the seismic cycle. Here also, numerous small-scale velocity-weakening patches could explain the occurrence of seismic swarms on the edges of the intersegment and in particular beneath the Caldera Peninsula where coupling is intermediate.

## 6 CONCLUSION

New horizontal and vertical data in the North-Central Chile area (34°S to 25°S) are used together with older data sets to invert simultaneously for along-strike coupling variations on the subduction plane and for the motion of an Andean rigid block relative to stable South America. We find that the inclusion of a rigid sliver block that moves  $\sim 5$  mm yr<sup>-1</sup> towards northeast improves the fit to the data, and that important lateral variations in the coupling

amount are needed to fit the upper-plate deformation pattern, whatever the rigid block motion is. These variations draw a coupling segmentation based on the along-strike changes of the average coupling, and highlight three highly coupled segments (Metropolitan, Atacama and Chañaral) and three weakly coupled intersegments (San Antonio, La Serena and Baranquilla).

This segmentation is consistent with the seismotectonic segmentation of the margin: highly coupled segments correlate with historical megathrust ruptures, while low-coupled intersegments correlate with zones that behave as barriers to the seismic rupture propagation and with the subduction of fracture zones or seamounts. These intersegments often correlate with bays in the coastal shape, while intermediate coupling zones that bound the intersegments are associated with peninsulas below which seismic swarms occur and background seismicity is high. Therefore, if the apparent coupling reflects the mechanical behaviour of the interface, intersegments would stand for velocity-strengthening patches able to creep and slow down (even stop) major ruptures, while segments would stand for velocity-weakening patches able to rupture coseismically. Peninsulas would therefore correlate with a patchwork of small-scale asperities able to generate swarms.

The Metropolitan segment yet described by Métois *et al.* (2012) does not match the standard description of a ‘seismic gap’ that should release all the cumulated deformation and break with a single megathrust earthquake, because the present-day background seismicity rate is high and has been increased by the post-seismic motion triggered by the Maule earthquake. Nonetheless, it can generate smaller subduction earthquakes ( $M_w \leq 8$ ) that correspond to the rupture of one single asperity. Similarly, based on the historical seismicity in the northern part of our network (north of 30°S) and following Beck *et al.* (1998), we propose that the northernmost Atacama and Chañaral segments can either rupture alone with 1983-type intermediate depth  $M_w \leq 8$  earthquakes that typically occur every ~40 yr, or rupture together with a 1922-type megathrust  $M_w > 8$  earthquake. In this case, the rupture would be complex, potentially rich in high-frequency content, since it has to propagate through the Baranquilla intersegment thought to be composed of small-scale velocity-weakening asperities, and should also rupture the shallowest part of the subduction interface producing important tsunamis. Therefore, it is plausible that these multiple-segment rupture scenarios are part of a ‘super-cycle’ of megathrust earthquakes that would occur only once a century in the North-Central Chile, on top of the shorter cycle of moderate earthquakes.

## ACKNOWLEDGEMENTS

This work was performed in the frame of the French–Chilean LIA ‘Montessus de Ballore’ with financial support of the CNRS/INSU, U-Chile and ANR grant ‘MEGA-Chile’. We would like to thank R. McCaffrey for freely providing the DEFNODE code and GFZ and OSU for giving access to their markers (SAGA and CAP projects) and to data produced by several of their cGPS stations in Chile. Most figures of this paper were generated using the free Generic Mapping Tools software (GMT). We are grateful to many people who participated in measurement campaigns, especially students from DGF, IGP and ENS. We would like to thank IRD Chile for providing us with facilities on the field. We would like to thank M. Moreno and an anonymous reviewer for thorough reviews of this paper. This is IGP contribution 3436.

## REFERENCES

- Altamimi, Z., Collilieux, X. & Métivier, L., 2011. ITRF2008: an improved solution of the International Terrestrial Reference Frame, *J. Geod.*, **85**(8), 457–473.
- Angermann, D. & Klotz, J., (1999). Space-geodetic estimation of the Nazca–South America Euler vector, *Earth planet. Sci. Lett.*, **171**, 329–334.
- Arriagada, C., Roperch, P., Mpodozis, C. & Cobbold, P., 2008. Paleogene building of the Bolivian Orocline: tectonic restoration of the central Andes in 2-D map view, *Tectonics*, **27**(6), TC6014, doi:10.1029/2008TC002269.
- Beck, S., Barrientos, S. & Kausel, E., 1998. Source characteristics of historic earthquakes along the central Chile subduction zone, *J. S. Am. Earth Sci.*, **11**(2), 115–129.
- Béjar-Pizarro, M. *et al.*, 2010. Asperities and barriers on the seismogenic zone in North Chile: state-of-the-art after the 2007 Mw 7.7 Tocopilla earthquake inferred by GPS and InSAR data, *Geophys. J. Int.*, **183**(1), 390–406.
- Beutler, G., Rothacher, M. & Schaer, S., 1999. The International GPS Service (IGS): an interdisciplinary service in support of earth sciences, *Adv. Space*, **23**(4), 631–653.
- Brooks, B.A., Bevis, M., Smalley, R. Jr, Kendrick, E., Manceda, R., Lauría, E., Maturana, R. & Araujo, M., 2003. Crustal motion in the Southern Andes (26°–36°S): do the Andes behave like a microplate? *Geochem. Geophys. Geosyst.*, **4**(10), 1–14.
- Brooks, B.A. *et al.*, 2011. Orogenic-wedge deformation and potential for great earthquakes in the central Andean backarc, *Nat. Geosci.*, **4**(6), 380–383.
- Chlieh, M. *et al.*, 2011. Interseismic coupling and seismic potential along the Central Andes subduction zone, *J. geophys. Res.*, **116**(B12), 1–21.
- Comte, D. & Pardo, M., 1991. Reappraisal of great historical earthquakes in the northern Chile and southern Peru seismic gaps, *Nat. Hazards*, **4**(1), 23–44.
- Comte, D., Haessler, H., Dorbath, L., Pardo, M., Monfret, T., Lavenue, A., Pontoise, B. & Hello, Y., 2002. Seismicity and stress distribution in the Copiapo, northern Chile subduction zone using combined on- and off-shore seismic observations, *Phys. Earth planet. Inter.*, **132**(1–3), 197–217.
- Deschamps, A., Lyon-Caen, H. & Madariaga, R., 1980. Etude du tremblement de terre de Taltal (Chili, 1966) à partir des ondes sismiques de longue période, *Ann. Geophys.*, **36**(2), 179–190.
- DeMets, C., 1994. Effect of recent revision to the geomagnetic reversal time scale on estimates of current plate motions, *Geophys. Res. Lett.*, **2**(20), 2191–2194.
- DeMets, C., Gordon, R.G. & Argus, D.F., 2010. Geologically current plate motions, *Geophys. J. Int.*, **181**(1), 1–80.
- Ducret, G., Doin, M.P., Grandin, R., Socquet, A., Vigny, C., Métois, M. & Béjar-Pizarro, M., 2012. Measurement of interseismic strain accumulation in the southern Andes (25–35 s) using Envisat Sar data, in *Proceedings of EGU General Assembly Conference Abstracts*, Vol. 14, p. 10391.
- Gardi, A., Lemoine, A., Madariaga, R. & Campos, J., 2006. Modeling of stress transfer in the Coquimbo region of central Chile, *J. geophys. Res.*, **111**(B4), 1–10.
- Herring, T.A., 2002. *Gloabk: Global Kalman filter VLBI and GPS Analysis Program, Version 10.0*, Massachusetts Institute of Technology.
- Holtkamp, S.G., Pritchard, M.E. & Lohman, R.B., 2011. Earthquake swarms in South America, *Geophys. J. Int.*, **187**(1), 128–146.
- Jordan, T.E. & Allmendinger, R.W., 1986. The Sierras Pampeanas of Argentina: a modern analogue of Rocky Mountain foreland deformation, *Am. J. Sci.*, **286**(10), 737–764.
- Kadinsky-Cade, K., Reilinger, R. & Isacks, B., 1985. Surface deformation associated with the November 23, 1977, Caucaete, Argentina, earthquake sequence, *J. geophys. Res.*, **90**(14), 12–691.
- Khazaradze, G. & Klotz, J., 2003. Short- and long-term effects of GPS measured crustal deformation rates along the south central Andes, *J. geophys. Res.*, **108**(B6), 1–13.
- King, R.W. & Bock, Y., 2002. *Documentation for the GAMIT Analysis Software, Release 10.0*, Massachusetts Institute of Technology.



- Lomnitz, C., 2004. Major Earthquakes of Chile: a Historical Survey, 1535–1960, *Seismol. Res. Lett.*, **75**, 368–378.
- Loveless, J.P. & Meade, B.J., 2011. Spatial correlation of interseismic coupling and coseismic rupture extent of the 2011  $M_w = 9.0$  Tohoku-oki earthquake, *Geophys. Res. Lett.*, **38**, L17306, doi:10.1029/2011GL048561
- McCaffrey, R., 2002. Crustal block rotations and plate coupling, plate boundary zones, *Geodyn. Ser.*, **30**, doi:10.1029/GD030p0101
- McQuarrie, N., 2002. The kinematic history of the central Andean fold-thrust belt, Bolivia: implications for building a high plateau, *Geol. Soc. Am. Bull.*, **114**(8), 950–963.
- Métois, M., Socquet, A. & Vigny, C., 2012. Interseismic coupling, segmentation and mechanical behavior of the central Chile subduction zone, *J. geophys. Res.*, **117**(B03406), doi:10.1029/2011JB008736.
- Métois, M. *et al.*, 2013. Revisiting the North Chile seismic gap segmentation using GPS-derived interseismic coupling, *Geophys. J. Int.*, **194**(3), 1283–1294.
- Niell, A.E., 1996. Global mapping functions for the atmosphere delay at radio wavelengths, *J. geophys. Res.*, **101**(B1), 3227–3246.
- Pardo, M., Comte, D. & Monfret, T., 2012. Seismotectonic and stress distribution in the central Chile subduction zone, *J. South Am. Earth Sci.*, **15**(1), 11–22.
- Perfettini, H. *et al.*, 2010. Seismic and aseismic slip on the Central Peru megathrust, *Nature*, **465**(7294), 78–81.
- Ruegg, J. *et al.*, 2009. Interseismic strain accumulation measured by GPS in the seismic gap between Constitución and Concepción in Chile, *Phys. Earth planet. Inter.*, **175**(1–2), 78–85.
- Scholz, C.H. & Small, C., 1997. The effect of seamount subduction on seismic coupling, *Geology*, **25**(6), 487–490.
- Tassara, A., Gotze, H.J., Schmidt, S. & Hackney, R., 2006. Three-dimensional density model of the Nazca plate and the Andean continental margin, *J. geophys. Res.*, **111**(B9), doi:10.1029/2005JB003976
- Vigny, C., Rudloff, A., Ruegg, J.-C., Madariaga, R., Campos, J. & Alvarez, M., 2009. Upper plate deformation measured by GPS in the Coquimbo Gap, Chile, *Phys. Earth planet. Inter.*, **175**(1–2), 86–95.
- Vigny, C. *et al.*, 2011. The 2010  $M_w$  8.8 Maule megathrust earthquake of Central Chile, monitored by GPS, *Science*, **332**(6036), 1417–1421.
- Wang, K. & Bilek, S.L., 2011. Do subducting seamounts generate or stop large earthquakes? *Geology*, **39**(9), 819–822.
- Willis, B. & Macelwane, J.B., 1929. *Earthquake Conditions in Chile*. Carnegie Institution.

## SUPPORTING INFORMATION

Additional Supporting Information may be found in the online version of this article:

**Figure S1:** Left : time series of four continuous stations of our Norte Chico network imaging the coseismic and postseismic signal associated to Maule event on the North component, if so. Right : coseismic jump measured on permanent stations by Vigny *et al.* (2011) (orange vectors), and interpolated jump on each benchmark (black arrows).

**Figure S2:** Large scale network and far field velocities. Dots show locations of GPS stations. Arrows depict their horizontal velocities with respect to a reference frame fixed on the South-America plate tied by the reddot stations. Bold numbers aside the arrows indicate the velocity in mm/yr. Ellipses depict the region of 99% confidence.

**Figure S3:** Sensitivity of horizontal (left) and vertical (right) data collected over our network to unit coupling on the  $20^\circ$  dipping slab. Each element of the interface is colored by the log of the sum of the displacements (P in mm/yr) at GPS stations (dots) due to unit slip on the nearest grid node.

**Figure S4:** Coupling patterns inverted for a 3-plate model and with different constrains on coupling at shallow depth. The smoothing coefficient is fixed to  $0.7^\circ$ , and no coupling is allowed under 80 km

depth. From left to right : no constrain on shallow coupling, locking of the surface node only, locking of the whole interface from 0 to 7 km depth, locking of the whole interface from 0 to 12 km depth. The normalized root mean square (nRMS) is indicated in the upper right corner of each plot.

**Figure S5:** Checkerboard resolution tests. From left to right : coupling checkerboard pattern used to generate a synthetic deformation field; coupling distribution retrieved by an inversion of the raw synthetic velocities without smoothing constrain; coupling distribution retrieved by the inversion of the synthetic velocity field in which random noise ( $\pm 2$  mm/yr in average) has been added; same but adding an increasing with depth smoothing constrain ( $0.7^\circ$ ) which smears the small scale original checkerboard.

**Figure S6: 2-Plate model/varying smoothing values** Coupling patterns inverted using different initial smoothing values. Coupling is color coded as in Fig. 5. The smoothing value and the normalized root mean square relative to horizontal (hRMS) or vertical (vRMS) data are indicated in the upper right corner of each plot. We plot the variations of nRMS with smoothing in the bottom right corner of the smoothest inversion

**Figure S7: 2-Plate model/varying smoothing values/ddc constrain** Same caption as fig. 6, but with “ddc” constrain that forces coupling to decrease with depth.

**Figure S8: 3-Plate model/varying smoothing values** Same caption as fig. 6 but for 3-plate models. The sliver poles found for each inversion are listed in table 8.

**Figure S9: 3-Plate model/varying smoothing values/ddc constrain** Same caption as figure 8, but with “ddc” constrain that forces coupling to decrease with depth.

**Figure S10:** Coupling distribution inverted using various Nazca-South America convergence velocities, with  $0.7^\circ$  smoothing coefficient that increases with depth, no coupling allowed under 80 km depth, in a 3-plate configuration. From left to right : coupling distribution obtained with increasing relative velocities described by the ITRF 2005, Vigny *et al.* (2009) and MORVEL (DeMets *et al.*, 2010) poles.

**Figure S11:** Coupling distribution inverted using different data sets, with  $0.7^\circ$  smoothing coefficient that increases with depth, no coupling allowed under 80 km depth, in a 3-plate configuration. From left to right : coupling distribution inverted using all available horizontal and vertical velocities, same but using only the more recent data set published in this study (LiA-MdB), coupling distribution inverted using all available horizontal velocities only.

**Table S1:** Horizontal velocities in mm/yr on our campaign network. Vlat and Vlon are given either in the ITRF 2008 reference frame (columns 3 and 4), or in the NNR-Nuvel1A South-America fixed reference frame (columns 5 and 6).

**Table S2:** Horizontal velocities in mm/yr on permanent stations used to stabilize the processing. Sites used to constrain the reference frame are marked by the \* symbol. Note that only pre-Maule data from LPGS were used to constrain the reference frame. Stations are either from IGS network<sup>i</sup>, French-Chilean network<sup>f</sup>, RAMSAC Argentine network<sup>a</sup>, or RBMC Brazilian network<sup>b</sup>.

**Table S3:** Vertical velocities in mm/yr selected on several quality criteria, for the inversion process.

**Table S4:** Table of measurement for each campaign since 2004.

**Table S5:** Repeatability for each campaign on North, East and vertical components.

**Table S6:** Applied coseismic jump (in mm) on North, East and Vertical direction on campaign points located north of 30S. Estimations from interpolation of coseismic jumps measured at permanent stations (Vigny *et al.*, 2011).



**Table S7:** Summary of published poles for the Nazca-South America relative motion using either geological methods (top) or GPS velocities only (bottom). The average velocity predicted by each pole at 30° S (i.e the center of our study area) is indicated in the last column (in mm/yr).

**Table S8:** Normalized RMS, Andean sliver pole and average horizontal motion produced by block rotation on our network, depending on the constrains imposed in each 3-plate model tested.

**Table S9:** Average convergence between Nazca and South America, normalized RMS, Andean sliver pole and average horizontal

motion produced by block rotation on our network, depending on the Nazca-South American relative pole imposed in our 3-plate models (fig. 10).

(<http://gji.oxfordjournals.org/lookup/suppl/doi:10.1093/gji/ggt418/-/DC1>)

Please note: Oxford University Press are not responsible for the content or functionality of any supporting materials supplied by the authors. Any queries (other than missing material) should be directed to the corresponding author for the article.